Atmos. Chem. Phys. Discuss., https://doi.org/10.5194/acp-2018-1116
Manuscript under review for journal Atmos. Chem. Phys.
Discussion started: 16 January 2019

Atmospheric Chemistry and Physics
Discussions

Analysis of Total Column CO_2 and CH_4 Measurements in Berlin with WRF-GHG

Xinxu Zhao[1], Julia Marshall[2], Stephan Hachinger[3], Christoph Gerbig[2], and Jia Chen[1]

[1]Electrical and Computer Engineering, Technische Unversität München, 80333 Munich, Germany
[2]Max Plank Institute of Biogeochemistry, 07745 Jena, Germany
[3]Leibniz Supercomputering Center (Leibniz-Rechenzenturm, LRZ) of Bavarian Academy of Sciences and Humanities, Bolzmannstr. 1, 85748 Garching, Germany

Correspondence: Jia Chen (jia.chen@tum.de)

Abstract. Though they cover less than 3 % of the global land area, urban areas are responsible for over 70 % of the global greenhouse gas (GHG) emissions and contain 55 % of the global population. A quantitative tracking of GHG emissions in urban areas is therefore of great importance, with the aim of accurately assessing the amount of emissions and identifying the emission sources. The Weather Research and Forecasting model (WRF) coupled with GHG modules (WRF-GHG) developed for mesoscale atmospheric GHG transport, can predict column-averaged abundances of CO_2 and CH_4 (XCO_2 and XCH_4). In this study, we use WRF-GHG to model the Berlin area at a high spatial resolution of 1 km. The simulated wind and concentration fields were compared with the measurements from a campaign performed around Berlin in 2014 (Hase et al., 2015). The measured and simulated wind fields mostly demonstrate good agreement and the simulated XCO_2 agrees well with the measurement. In contrast, a bias in the simulated XCH_4 of around 2.7 % is found, caused by relatively high initialization values for the background concentration field. We find that an analysis using differential column methodology (DCM) works well for the XCH_4 comparison, as corresponding background biases then cancel out. From the tracer analysis, we find that the enhancement of XCH_4 is highly dependent on human activities. The XCO_2 signal in the vicinity of Berlin is dominated by anthropogenic behavior rather than biogenic activities. We conclude that DCM is an effective method for comparing models to observations independently of biases caused, e.g., by initial conditions. It allows us to use our high resolution WRF-GHG model to detect and understand sources of GHG emissions quantitatively in urban areas.

Atmos. Chem. Phys. Discuss., https://doi.org/10.5194/acp-2018-1116
Manuscript under review for journal Atmos. Chem. Phys.
Discussion started: 16 January 2019

1 Introduction

The share of greenhouse gas (GHG) emissions released from urban areas has continued to increase as a result of urbanization (IEA, 2008; Kennedy et al., 2009; Parshall et al., 2010; IPCC, 2014). At present 55 % of the global population resides in urban areas (UNDESA, 2014), a number that is projected to rise to 68 % by 2050 (UNDESA, 2018). Meanwhile urban areas cover less than 3 % of the land surface worldwide (Wu et al., 2016), but consume over 66 % of the world's energy (Fragkias et al., 2013), and generate more than 70 % of anthropogenic GHG emissions (Hopkins et al., 2016). Carbon dioxide (CO_2) emissions from energy use in cities are estimated to comprise more than 75 % of the global energy-related CO_2, with a rise of 1.8 % per year projected under business-as-usual scenarios between 2006 and 2030 (IEA, 2009). Methane (CH_4) emissions from energy, waste, agriculture, and transportation in urban areas make up approximately 21 % of the global CH_4 emissions (Marcotullio et al., 2013; Hopkins et al., 2016). As emission hotspots, urban areas therefore play a vital role in GHG mitigation. It is crucial to find appropriate methods for understanding and projecting the effects of GHG emissions on urban areas, and for formulating mitigation strategies.

There are two methods for the quantitative analysis of GHG emissions: the 'bottom-up' approach and the 'top-down' approach (Pillai et al., 2011; Caulton et al., 2014; Newman et al., 2016). The 'bottom-up' approach calculates emissions based on activity data (i.e., a quantitative measure of the activity that can emit GHGs) and emission factors (Wang et al., 2009). This approach has some uncertainty, e.g., on the national fossil-fuel CO_2 emissions, reaching a maximum of over 50 % in extreme cases (Andres et al., 2012). The considerable uncertainties are caused by the large variability of source-specific and country-specific emission factors and the incomplete understanding of emission processes (Montzka et al., 2011; Bergamaschi et al., 2015). These uncertainties grow larger at sub-national scales, when estimating the disaggregation of the national annual totals in space and time. The 'top-down' approach utilizes GHG observations along with inverse models to estimate atmospheric fluxes. Though the 'top-down' approach can provide estimated global fluxes and independent assessments of inventory-based emission magnitudes (Montzka et al., 2011), it is hard to quantify the statistical errors attached to both atmospheric observations and prior knowledge about the distribution of emissions and sinks (Cressot et al., 2014).

McKain et al. (2012) suggested that column measurements can provide a promising route to improving the detection of CO_2 emitted from major source regions, possibly avoiding extensive surface measurements near such regions. Such measurements, i.e. measurements of concentration averaged over a column of air, are performed to help to disentangle the effects of atmospheric mixing from the surface exchange (Wunch et al., 2011) and decrease the biases associated with carbon cycle processes in atmospheric inversions (Olsen and Randerson, 2004). Compared to surface values, urban enhancements in columns are less sensitive to boundary-layer heights (Wunch et al., 2011; McKain et al., 2012; Kivi and Heikkinen, 2016) and column observations have the potential to mitigate mixing height errors in an atmospheric inversion system (Gerbig et al., 2008). Atmospheric GHG column measurements combined with inverse models are thus a promising method for analyzing GHG emissions, and can be used to analyze their spatial and temporal variability (Ohyama et al., 2009; Pillai et al., 2011; Ostler et al., 2016; Kivi and Heikkinen, 2016).

Atmos. Chem. Phys. Discuss., https://doi.org/10.5194/acp-2018-1116
Manuscript under review for journal Atmos. Chem. Phys.
Discussion started: 16 January 2019

Atmospheric Chemistry and Physics Discussions

In order to focus the 'top-down' approach on concentration differences caused by local and regional emission sources, and in particular to quantify urban emissions, the differential column methodology (DCM) was proposed. It evaluates differences between column measurements at different sites. Chen et al. (2016) applied the DCM using compact Fourier Transform Spectrometer (FTS) EM27/SUN and demonstrated the capability of differential column measurements for determining urban and local emissions in combination with column models. Citywide GHG column measurement campaigns have been carried out, e.g., in Boston (Chen et al., 2013), Indianapolis (Franklin et al., 2017), San Francisco, Berlin (Hase et al., 2015), and Munich (Chen et al., 2018). However, only a few studies have combined differential column measurements with high-resolution models. Toja-Silva et al. (2017) simulated the column data at upwind and downwind sites of a gas-fired power plant in Munich using the Computational Fluid Dynamic model (CFD) and compared them with the column measurements. Viatte et al. (2017) quantified CH_4 emissions from the largest dairies in the southern California region, using four EM27/SUNs in combination with the Weather Research and Forecasting model (WRF) in large-eddy simulation mode. Vogel et al. (2018) deployed five EM27/SUN in the Paris metropolitan area and analyzed the data with the atmospheric transport model framework CHIMERE-CAMS.

This paper carries out a quantitative analysis of GHG for the Berlin area in combination with DCM. We utilize the mesoscale WRF model (Skamarock et al., 2008) coupled with GHG modules (WRF-GHG) (Beck et al., 2011) at a high resolution of 1 km. The aim is to assess the precision of WRF-GHG and to provide insights on how to detect and understand sources of GHGs (CO_2 and CH_4) within urban areas. WRF is a numerical weather prediction system and can be used for both atmospheric research and operational forecasting, on a mesoscale range from tens of meters to thousands of kilometers, cf. e.g. (Chen et al., 2011). To produce high-resolution regional simulations of atmospheric CH_4 passive tracer transports, WRF was coupled with the Vegetation Photosynthesis and Respiration module (WRF-VPRM) (Ahmadov et al., 2007). WRF-VPRM has been widely employed in several studies, in which both the generally good agreement of the simulations with measurements and model biases have been assessed in detail (Ahmadov et al., 2009; Pillai et al., 2011, 2012; Kretschmer et al., 2012). WRF-VPRM was later extended to WRF-GHG (Beck et al., 2011), which can simulate the regional passive tracer transport for GHGs (CH_4, CO_2 and carbon monoxide (CO)). Relatively few studies using WRF-GHG have been published as yet, e.g., the simulation of CO_2 mixing ratios for a domain centered over Berlin at a high spatial resolution of 10 km (Pillai et al., 2016). In the present paper, we focus on a high-resolution study of both CO_2 and CH_4 in Berlin, and adapt the simulation workflow to this purpose where needed.

The total annual CO_2 emissions of Berlin (21.3 million tonnes in 2010) approximately correspond to those of Croatia, Jordan or the Dominican Republic, and the Senate of Berlin is making efforts to transform the city into a climate neutral city (Reusswig and Lass, 2014). Berlin therefore needs to assess and identify the emission sources accurately at the current stage, to provide solid scientific support for the selection of mitigation options. Additionally, Berlin is an ideal pilot case for developing and testing simulations because the city is relatively isolated from other large cities with high emissions, such that anthropogenic GHG anomalies around Berlin can confidently be attributed to the city itself.

The major goals of our work in this context are: (1) to simulate high-resolution (1 km) CO_2 and CH_4 concentrations for Berlin using WRF-GHG, attributing the changes in concentrations to different emission processes; (2) to compare the simulation outputs with the observations from a column measurement network in Berlin (Hase et al., 2015), assessing the precision of

Atmospheric Chemistry and Physics
Discussions

WRF-GHG; (3) to use DCM in the simulation analysis, testing the feasibly of this approach. The structure of this paper is as follows: The model with its domain and external data sources are described in Sect.2. A comparison analysis for wind fields and concentration fields is presented in Sect.3, and CO_2 and CH_4 concentrations related to different processes (e.g., the anthropogenic component) are discussed. DCM for the comparison of concentration fields and the tracer analysis is presented and discussed in Sect.4. Section 5 provides the discussion and summary of this study.

2 WRF-GHG Modeling System

As mentioned in Sect.1, we use the WRF model Version 3.2 coupled with GHG modules to quantify the uptake and emission of atmospheric GHGs around Berlin at a high resolution of 1 km. WRF follows the fully compressible nonhydrostatic Euler equations (Skamarock et al., 2005, 2008) and is based on the actual meteorological conditions in this case study. Tracers in WRF-GHG are transported online in a passive way, i.e. without any chemical loss or production, when the tracer transport option is used (Ahmadov et al., 2007; Beck et al., 2011). As shown in Fig.1, three domains are set up here, whose dimensions are 70 × 50 horizontal grid points with a spacing of 9 km for the coarsest domain (d01), 3 km for the middle domain (d02) and 1 km for the innermost domain (d03). WRF uses a terrain-following hydro-static pressure vertical coordinate (Skamarock et al., 2008). In our case, 26 vertical levels are defined from the surface up to 50 hPa, 14 of which are in the lowest 2 km of the atmosphere. The innermost domain, d03, envelops all five measurement sites (see Sect.3.1) to assess the simulation by comparing with the measured data. Berlin lies in the North European Plain on flat land (crossed by northward-flowing water-courses), which avoids the vertical interpolation problems caused by topography differences (Fig.1). The Lambert conformal conic projection is selected as map projection. The simulated time span is from 18 UTC on 30$^{\text{th}}$ June to 00 UTC on 11$^{\text{th}}$ July in 2014. The description of the workflow for running WRF-GHG can be found in Appendix A.

The meteorological fields are obtained from the Global Forecast System model (GFS) at a horizontal resolution of 0.5° with 64 vertical layers and a temporal resolution of 3 hours (as available via the NOAA-NCDC/NCEI, www.ncdc.noaa.gov). The GFS uses hydrostatic equations for the prediction of atmospheric conditions, and its output includes large amounts of atmospheric and land-soil variables, wind fields, temperature, precipitation and soil moisture etc. The initial and lateral boundary conditions for our WRF-GHG concentration fields are implemented using Copernicus Atmosphere Monitoring Service (CAMS) data (Agusti-Panareda et al., 2017). CAMS provides the estimated mixing ratios of CO_2 and CH_4 with a spatial resolution of 0.8° on 137 vertical levels, with a temporal resolution of 6 hours (as available via https://atmosphere.copernicus.eu).

The simulation of CO_2 and CH_4 fluxes with different emission tracers in WRF-GHG is based on flux models and emission inventories which are either already implemented inside the model modules ('online' calculation) or constitute external datasets ('offline' calculation). The flux values from external emission inventories are converted into atmospheric concentrations and added to the corresponding tracer variables. In combination with the background concentration fields for CO_2 and CH_4, the tracer contributions are summed up to obtain the total concentrations, as

$$\begin{aligned} CO_{2,\text{total}} &= CO_{2,\text{bgd}} + CO_{2,\text{VPRM}} + CO_{2,\text{anthro}} + \Delta CO_2 \\ CH_{4,\text{total}} &= CH_{4,\text{bgd}} + CH_{4,\text{anthro}} + CH_{4,\text{soil}} + \Delta CH_4 \end{aligned} \tag{1}$$

Atmos. Chem. Phys. Discuss., https://doi.org/10.5194/acp-2018-1116
Manuscript under review for journal Atmos. Chem. Phys.
Discussion started: 16 January 2019

Atmospheric Chemistry and Physics Discussions

where $CO_{2,total}$ and $CH_{4,total}$ represent the total CO_2 and CH_4, $CO_{2,bgd}$ and $CH_{4,bgd}$ are the background CO_2 and CH_4, $CO_{2,anthro}$ and $CH_{4,anthro}$ stand for the changes in CO_2 from the anthropogenic emissions, $CO_{2,VPRM}$ is the change in CO_2 from the biogenic activities and $CH_{4,soil}$ is the change in CH_4 from soil uptake, ΔCO_2 and ΔCH_4 are the tiny computational errors for CO_2 and CH_4 described in detail in Appendix B. In the transport process, the relationship shown in Eq.1 holds for each vertical level.

The biogenic CO_2 emission is calculated online using VPRM (Mahadevan et al., 2008), in which the hourly Net Ecosystem Exchange (NEE) of CO_2 reflects the biospheric fluxes between the terrestrial biosphere and the atmosphere, estimated by the sum of Gross Ecosystem Exchange (GEE) and Respiration. We use the external dataset Emission Database for Global Atmospheric Research Version 4.1 (EDGAR V.4.1) for the anthropogenic fluxes in our study. EDGAR V.4.1 provides annually varying global anthropogenic GHG emissions and air pollutants at a spatial resolution of 0.1° (Muntean et al., 2014; Janssens-Maenhout et al., 2015), whose source sectors include industrial processes, on-road and off-road sources in transport, large-scale biomass burning and other anthropogenic sources (Saikawa et al., 2017). Here we apply time factors for seasonal, daily and diurnal variations defined by the time profiles published on the EDGAR website (http://themasites.pbl.nl/tridion/en/themasites/edgar/documentation/content/Temporal-variation.html); however, considerable uncertainties are to be expected in applying these time factors. The chemical sink for atmospheric CH_4 can be ignored in the model owing to its relatively long lifespan (9.5 ± 1.3 year, Holmes (2018)), the small-scale domains, and the limited simulation period (10 days) in our case.

3 Model Analysis and Model-Measurement Comparison

3.1 Description of Measurement Sites

The measurement campaign used to compare with WRF-GHG in this paper was performed from 23rd June to 11th July 2014 in Berlin using five spectrometers (Hase et al., 2015). It allows us to both test the precision of WRF-GHG (Sect.3) and verify differential column methodology (DCM) as our analytic methodology (Sect.4). In their measurement campaign, Hase et al. (2015) used five portable Bruker EM27/SUN Fourier Transform Spectrometers (FTS) for atmospheric measurements based on solar absorption spectroscopy. Five sampling stations around Berlin were set up, four of which (Mahlsdorf, Heiligensee, Lindenberg and Lichtenrade) were roughly situated along a circle with a radius of 12 km around the center of Berlin. Another sampling site was closer to the city center and located inside the Berlin motorway ring at Charlottenburg (Fig.6). Detailed information on this measurement campaign is given in Hase et al. (2015).

3.2 Comparison of Wind Fields

Winds have a strong impact on the vertical mixing of GHGs and a direct influence on their atmospheric transport patterns. Hence, we firstly compare the wind speeds and wind directions obtained from WRF-GHG to the measurements, such that deviations between the simulated and measured wind fields are assessed. The wind measurements are not exactly co-located with the spectrometers mentioned in Sect.3.1, but rather are located at three sampling sites (Tegel, Schönefeld and Tempelhof, respectively) and measure at a height of 10 meters above the ground. The simulated wind speed at 10 meters (ws_{10m}) and wind

Atmos. Chem. Phys. Discuss., https://doi.org/10.5194/acp-2018-1116
Manuscript under review for journal Atmos. Chem. Phys.
Discussion started: 16 January 2019

direction at 10 meters (wd_{10m}) are calculated following the equations,

$$
\begin{aligned}
ws_{10\text{m}} &= \sqrt{u_{10\text{m}}^2 + v_{10\text{m}}^2} \\
wd_{10\text{m}} &= \arctan \frac{v_{10\text{m}}}{u_{10\text{m}}}
\end{aligned}
\tag{2}
$$

where $u_{10\text{m}}$ and $v_{10\text{m}}$ are the components of the horizontal wind, towards the east and north respectively, which can be obtained from WRF-GHG output files.

The time variations of the simulated and measured wind fields at 10 meters from 1$^{\text{st}}$ July to 5$^{\text{th}}$ July and the differences between models and measurements during these 5 days are shown in Fig.2. The measured (dotted lines) and simulated (solid lines) wind speeds (Fig.2(a)) at 10 meters show similar trends and demonstrate relatively good agreement over the 5-day time series with a square correlation coefficient of $R^2 = 0.6987$. Large uncertainties in wind speeds are found to appear always with the lower wind speeds, mostly at night. For wind directions, we observe that the simulated wind directions show similar but slightly underestimated fluctuations (Fig.2(b)), which result in a square correlation coefficient of $R^2 = 0.4235$. We find that a larger uncertainty in wind direction exists also during the low wind speed periods (Fig.2(a)&(b)). Compared to the simulations, the measured wind fields have more fluctuations. The discrepancies of wind fields between models ad measurements appear typically during the period between 15 UTC on 3$^{\text{rd}}$ July and 06 UTC on 4$^{\text{th}}$ July.

3.3 Comparison of pressure-weighted column-averaged concentrations

In the following, we use the measured concentration fields to compare with the simulated fields. An FTS EM27/SUN can measure the column-integrated amount of a tracer through the atmospheric column with excellent precision, yielding the column-averaged dry-air mole fractions (DMFs) of the target gases (Chen et al., 2016; Hedelius et al., 2016). The measured DMFs of CO_2 and CH_4 are denoted by XCO_2 and XCH_4. Averaging kernels from EM27/SUN instruments are similar and almost equal to one at all altitudes (Hedelius et al., 2016), and thus can be neglected in the comparison to the model output. Hase et al. (2015) used constant a priori profile shapes in the retrievals. In order to compare the simulated concentration fields with the observations, the simulated pressure-weighted column-averaged concentration for a target gas G (XG) is calculated as,

$$
\Delta p(i) = \frac{P(i) - P(i+1)}{P_{\text{sf}} - P_{\text{top}}} \rightarrow XG = \sum_{i=1}^{n} \Delta p(i) \times G_{\text{sim}}(i)
\tag{3}
$$

Here, Δp_i is the proportional to the differences of the pressure values $P(i)$ at the bottom and $P(i+1)$ at the top of the i^{th} vertical grid cell; P_{top} and P_{sf} represent the hydrostatic pressures at the top and at the surface of the model domain, and $G_{\text{sim}}(i)$ stands for the simulated concentration of the target gas G at the i^{th} vertical level.

According to Hase et al. (2015), the best-quality measurements were made on 3$^{\text{rd}}$ and 4$^{\text{th}}$ July. Figure.3 shows the measured and modelled variations of XCO_2 and XCH_4, and respective scatter plots for each gas on these two days. During these two days, the pressure-weighted column-averaged concentrations for CO_2 (XCO_2) show very good agreement with the measurements, indicated by a square correlation coefficient of $R^2 = 0.9136$, especially on 4$^{\text{th}}$ July (Fig.3(b)). While on 3$^{\text{rd}}$ July, the simulated concentrations are slightly higher than the observations (Fig.3(a)).

Figure.3(d) and (e) show the comparison of the pressure-weighted column-averaged concentrations for CH_4 (XCH_4) between observations and simulations on 3rd and 4th July. The simulated XCH_4 is around 1860 ppb while the measured value is around 1800 ppb which is comparable to the values (1790-1810 ppb) observed at two Total Carbon Column Observing Network (TCCON) measurement sites in June and July 2014, Bremen in Germany (Notholt et al., 2014) and Bialystok in Poland (Deutscher et al., 2014). There is an approximate offset of 50-60 ppb between observations and models. This bias of the simulated XCH_4 seems to be constant (around 2.7 %) each day. Thus we introduce an offset applied to all sites for each simulation date to compare the model and the measured data, effectively removing the bias, which we attribute to a too high background XCH_4. The daily offset is assumed to be the difference between the simulated and measured daily mean XCH_4. After applying the daily offset, the measured XCH_4 shows a somewhat better agreement with the simulation ($R^2 = 0.3729$, red squares in Fig.3(f)).

A major offset in modelled CH_4 background concentration fields could potentially be attributed to errors in the troposphere height, given the typical sharp decrease in the stratospheric CH_4 profile. However, the background concentration values of CAMS were directly fitted to the WRF pressure axis during the simulation, without the consideration of the actual WRF tropopause height, thus this is unlikely to be the case. An illustration of the vertical distribution for CH_4 is provided in Appendix C. In Sect.4, a DCM-based analysis is presented, which eliminates the bias from relatively high initialization values for the CH_4 background concentration field and makes it easier to assess WRF-GHG results with respect to the measurements.

3.4 Contributions of different sources and sinks to the total signal: Individual Emission Tracers

As described in Sect.2, the various flux models implemented in WRF-GHG are advected as separate tracers, making it possible to distinguish the signals in concentration space for different source and sink categories for CO_2 and CH_4 (Beck et al., 2011). Berlin is located in an area of low-lying, marshy woodlands with a mainly flat topography (Kindler et al., 2018). There is no wetland in Berlin according to the MODIS Land Cover Map (Friedl et al., 2010). The land covered by forests, green and open spaces (e.g., farmlands, parks, allotment gardens) accounts for 35 % of the total area in Berlin (SenStadtH, 2016). Additionally, eleven power plants are currently being operated in Berlin, eight of which have a capacity over 100 MW (Fraunhofer-Gesellschaft, 2018). In accordance with the geographical characteristics of the district and potential emission sources in Berlin, we focus on understanding the simulated emissions caused by vegetation photosynthesis and respiration ($XCO_{2,\mathrm{VPRM}}$) as well as anthropogenic activities ($XCO_{2,\mathrm{anthro}}$) for CO_2, and by soil uptake ($XCH_{4,\mathrm{soil}}$) as well as human activities ($XCH_{4,\mathrm{anthro}}$) for CH_4.

As an instructive example of an analysis involving these tracers, we look at the diurnal cycle of contributions from the different tracers mentioned above in Charlottenburg (Fig.4). The mean values, averaged over 9 days (from 2nd to 10th July) as well as a 95 % confidential interval calculated in the averaging process are shown in Fig. 4. Figure.4(a) clearly shows a decline during the day and a rise at night in the XCO_2 enhancement over the background, with a maximum decrease over the course of the day of around 2 ppm. The XCO_2 enhancement over the background (blue: $XCO_{2,\mathrm{total}}$ - $XCO_{2,\mathrm{bgd}}$) reaches its daily peak during morning rush hour (07 UTC). The morning peak corresponds to XCO_2 changes from human activities, depicted by the black line from 04 UTC to 07 UTC (marked by a red square in Fig.4(a)). Before the evening rush hour (16 UTC), XCO_2 over the background then decreases, owning to biogenic uptake. Beginning in the evening, values increase again. Wiggles in the evening (17 UTC – 19 UTC) are dominated by XCO_2 enhancements from human activities while the substantial rise from 19 UTC onward is generated by the VPRM tracer, specifically the accumulation of the vegetation respiration in the evening.

The biogenic component plays a pivotal role in the variations of the XCO_2 enhancements. The anthropogenic impact on XCO_2 is weaker compared to the strong biogenic uptake. To further highlight the role of anthropogenic activities in XCO_2 changes and quantify anthropogenic emissions, DCM is applied in Sect.4. More specifically, we will use downwind-minus-upwind column differences of CO_2 (ΔXCO_2) to describe the XCO_2 enhancement over an upwind site, as the difference between the downwind and upwind sites can be attributed to urban emissions.

Turning to XCH_4 in Fig.4(b), we plot the variations of the mean hourly contributions from the anthropogenic (black line: $XCH_{4,\text{anthro}}$) and soil uptake tracer (blue: $XCH_{4,\text{soil}}$) in Charlottenburg. The contributions by anthropogenic activities fluctuate slightly around 2 ppb in the morning and at noon; then a peak occurs at the start of the evening rush hour (16 UTC). After 18 UTC, values clearly decrease, reaching approximately 2 ppb. From 21 UTC XCH_4 stabilizes, exhibiting only moderate fluctuations. The XCH_4 enhancement above the background (green: $XCH_{4,\mathrm{total}}$ - $XCH_{4,\mathrm{bgd}}$) depends largely on the XCH_4 contributions by human activities. The changes in concentrations caused by the soil uptake tracer (blue), whose values fluctuate between 0.001 ppb and 0.01 ppb, have almost no influence on the variation of the XCH_4 enhancement over background in the urban area.

Comparing the behavior of XCO_2 tracer contributions at different measurement sites (Fig.5(a)), we can see that VPRM tracer values follows a similar trend. There is obviously little difference in the biogenic contribution of XCO_2 across the five sampling sites. Compared to the other sites, XCO2 changes from human activities in Charlottenburg and Lichtenrade on 3rd July are higher (Fig.5(b)). As will be discussed in Sect.4.1 and Eq.6, Charlottenburg and Lichtenrade are downwind sites on 3rd July. The downwind sites during the day on 2nd July are Charlottenburg and Heiligensee, again the corresponding XCO_2 changes caused by the anthropogenic tracer in these two sampling sites are higher than elsewhere. As expected, XCO_2 changes from human activities at the downwind sites are higher than those at the upwind.

4 Model Analysis using Differential Column Methodology

4.1 Comparison of differential column concentrations

The differential column methodology (DCM) can be employed to detect and estimate local emission sources within an area, based on calculated concentration differences between downwind and upwind sites (Chen et al., 2016). The difference (ΔXG) of a specific gas G in column-averaged DMFs across the downwind and upwind sites is defined as,

$$\Delta XG = XG_{\text{downwind}} - XG_{\text{upwind}} \tag{4}$$

where XG_{downwind} and XG_{upwind} represent the column-average DMFs at the downwind and upwind sites.

In this study, DCM is applied to measurements and models in the spirit of a post-processing analysis. This approach is not only useful to cancel out the bias of the simulated XCH_4 (see Sect.3.3), but also to assess the role of anthropogenic activities in XCO_2 changes more appropriately.

A necessary prerequisite for DCM is distinguishing the upwind and downwind sites among all five sampling sites. Wind direction thus plays a pivotal role in the calculation of the downwind-minus-upwind column differences. In this study, the hourly simulated wind directions at the height of 10 meters are assumed as a standard to classify the sites into downwind and upwind sites.

The wind directions on 1st and 2nd July are more stable compared to the other simulation dates (cf. Fig.2(b)). In the interest of increasing our sample size, we take 1st, 2nd and 3rd July as dates to test our methodology on. East wind is the prevailing wind direction within the measurement period (from 06 UTC to 14 UTC) on 1st and 2nd July. Mahlsdorf and Lindenberg are upwind sites, and the downwind sites corresponding to these are Charlottenburg and Heiligensee (Fig.6). The wind direction on 3rd July mostly fluctuates between 0 and 90 degrees during the daytime; thus, the prevailing wind direction is more or less northeast. The upwind sites are Heiligensee and Mahlsdorf, and the corresponding downwind sites are Charlottenburg and Lichtenrade. Differential column concentrations (ΔXCH_4) on 1st, 2nd and 3rd July are, therefore, respectively calculated as:

East Wind (1st and 2nd July):

$$\begin{aligned}\Delta XCH_4^1 &= XCH_4^{\text{Heiligensee}} - XCH_4^{\text{Lindenberg}} \\ \Delta XCH_4^2 &= XCH_4^{\text{Charlottenburg}} - XCH_4^{\text{Mahlsdorf}}\end{aligned} \tag{5}$$

Northeast Wind (3rd July) :

$$\begin{aligned}\Delta XCH_4^1 &= XCH_4^{\text{Charlottenburg}} - XCH_4^{\text{Lindenberg}} \\ \Delta XCH_4^2 &= XCH_4^{\text{Lichtenrade}} - XCH_4^{\text{Mahlsdorf}}\end{aligned} \tag{6}$$

Figure.7(a), (b) and (c) depict the measured and simulated XCH_4 at the downwind and upwind sites on 1st, 2nd and 3rd July. The measured XCH_4 is shown in the 1st and 3rd rows while the sub-figures in the 2nd and 4th rows describe the simulated XCH_4. The XCH_4 at the downwind sites (black dots) are mostly higher than the values at the upwind sites (red dots) for both simulations and measurements. Sometimes, specifically for the measurements after 10 UTC on 3rd July, measured downwind values are lower than upwind values, which is unexpected. The phenomenon is not reproduced in the simulations. All this point to wind-fields patterns at that day such that the wind directions assumed in Eq.6, the simulated and the real wind directions deviate from one another. General trends in the measured XCH_4 values, such as the overall decrease from 08 UTC to 14 UTC on 3rd July, seem to be roughly reproduced by the simulations.

With a scatter plot in Fig.7(d), we illustrate the accuracy of the model with respect to the hourly mean ΔXCH_4. On 1st and 2nd July, the comparisons show good agreement, indicated by square correlation coefficients of $R^2 = 0.7878$ and $R^2 = 0.689$. On 3rd July, real hourly mean ΔXCH_4 values are often lower than the simulated values, which again may point towards inconsistencies in the wind directions (after 10 UTC) as discussed above. When we compare hourly simulated and measured XCH_4 only from 07 UTC to 10 UTC, we yield a square correlation coefficient of at least $R^2 = 0.454$. We conclude that DCM, as applied in this plot, reduces the model bias caused by the simulation initialization, but introduces unpleasant effects which may be attributed to errors in the assumed or simulated wind directions.

Yet, DCM as presented here has potential to highlight the role of anthropogenic activities, which we demonstrate applying it to CO_2 tracers in the simulation. We take 2^{nd} and 3^{rd} July as examples (Fig. 8). The prevailing wind on 2^{nd} July is easterly, since the simulated wind direction on 2^{nd} July is relatively stable, fluctuating only slightly between 65 and 130 degrees (Fig.8(a)). As described above, the prevailing wind direction on 3^{rd} July is, somewhat simplified, northeast (Fig.8(c)). We recall (Sect.3.4, Fig.5(b)) that Charlottenburg (2^{nd} July) and Lichtenrade (3^{rd} July) are the sites most affected by anthropogenic CO_2 emissions, while the sampling site with the least anthropogenic influence for both days is Lindenberg. In an explorative approach, we simply select Charlottenburg and Lichtenrade as the downwind sites on 2^{nd} and 3^{rd} July respectively, and choose Lindenberg as the upwind site for both days (Fig.6) for calculating the differential column concentrations,

$$\begin{aligned} &2^{\text{nd}}\ \text{July}: \Delta XCO_2 = XCO_2^{\text{Charlottenburg}} - XCO_2^{\text{Lindenberg}} \\ &3^{\text{rd}}\ \text{July}: \Delta XCO_2 = XCO_2^{\text{Lichtenrade}} - XCO_2^{\text{Lindenberg}} \end{aligned} \tag{7}$$

Figure.8 depicts the variations of the wind directions and ΔXCO_2 (corresponding to Eq.7) on 2^{nd} and 3^{rd} July. In contrast to XCO_2 values (Sect.3.4, Fig.4(a)), the simulated ΔXCO_2 (Fig.8(b)&(d), blue lines) is not so much influenced by the XCO_2 changes from the VPRM tracer (Fig.8(b)&(d), green), but more closely follows the XCO_2 changes from anthropogenic activities (Fig.8(b)&(d), red). With DCM, the role of human activities in XCO_2 changes is highlighted and the strong effect from the biogenic component is canceled out. The ΔXCO_2 measurements (Fig.8(b)&(d), black) show similar trends as the simulation, following the variation of the XCO_2 changes from anthropogenic activities.

4.2 Comparison between differential column concentrations and modeling results after the elimination of wind influence

As described in Sect.4.1, the wind direction impacts the distinction between downwind and upwind sites for DCM. Devising meaningful and accurate recipes for determining the wind directions is not easy, sometimes resulting in mixed-quality results (of Sect.4.1). Our simulated output provides the hourly wind and concentration fields. The instruments normally measure the concentration fields every minute. We simply assume the wind direction to be a constant value within one hour in our calculation, also when it comes to selecting up- and downwind sites. This may create inaccuracies in the calculation of the measured ΔXCH_4.

In this section, we test replacing the upwind values in DCM by an all-site mean to provide a potential solution for the elimination of such problems while still applying the DCM. The mean of the column-averaged DMFs over all sampling sites ($\overline{XG}_{\text{specific site}}$) is assumed to be the background concentration within the entire urban region, replacing the XCH_4 at the upwind site. The differences between the specific site and the mean of all the sites for each gas G ($\Delta\overline{XG}_{\text{specific site}}$) is then evaluated, i.e.

$$\Delta\overline{XG}_{\text{specific site}} = XG_{\text{specific site}} - \overline{XG}_{\text{all sites}} \tag{8}$$

where $XG_{\text{specific site}}$ is the column-averaged DMF at the respective sampling site.

We now test this form of DCM as follows: 1st July is taken as the test date and Charlottenburg, Heiligensee and Lichtenrade are chosen as test sites. The distance between any two sampling sites is around 25 km, and the variations of the XCH_4 at the three different sampling sites on the same day are almost the same (Fig.9(a),(b)&(c)). The sub-figures in the first row of Fig.9 depict the daytime cycle of the measured XCH_4 at the three sampling sites on 1st July and show several extreme values, e.g., in the period between 06 UTC and 07 UTC at Lichtenrade. The simulated XCH_4 (the second row of Fig.9) remains more stable compared to the measured XCH_4. This can be caused by underestimated emissions from anthropogenic activities and the smoothing of actual extreme values in the simulation. The general trends of the simulated and measured $\Delta\overline{\mathrm{XCH_4}}$ appear to be similar (the third row of Fig.9). Comparing $\Delta\overline{\mathrm{XCH_4}}$ from models and observations (Fig.9(d)), the simulations at the three sampling sites agree well with the measurements ($R^2 = 0.871$ in Charlottenburg, $R^2 = 0.8653$ in Heiligensee and $R^2 = 0.6129$ in Lichtenrade). With regards to the sampling sites, the measured and simulated $\Delta\overline{\mathrm{XCH_4}}$ in Lichtenrade show the best overlap (Fig.9(d)). A further analysis in a future study may provide deeper insight on site-specific transport characteristics.

As a final point in our analysis, we focus on simulated $\Delta\overline{\mathrm{XCO_2}}$ values (Fig.10). The $\Delta\overline{\mathrm{XCO_2}}$ (blue line) on 3rd, 4th, 5th and 6th July in Charlottenburg and Heiligensee are mainly dominated by the XCO_2 changes caused by the anthropogenic tracer (red), instead of the VPRM tracer (green). Compared to Fig.8(b)&(d), the red line and blue line in Fig.10 show a stronger similarity in their trends. With this form of DCM (compared to the original form in Sect.4.1), anthropogenic activities can be clearly shown to influence XCO_2 within urban areas.

5 Discussion and conclusion

We used WRF-GHG to quantitatively simulate the uptake, emission and transport of CO_2 and CH_4 for Berlin with a high resolution of 1 km. The simulated wind and concentration fields were compared with observations from 2014. Then, differential column methodology (DCM) was utilized as a post-processing method for the XCH_4 comparison and the XCO_2 tracer analysis.

The measured and simulated wind fields at 10 meters mostly demonstrate good agreement but with slight errors in the wind directions. The simulated XCO_2 concentrations actually reproduce the observations very well. Compared with the measured XCH_4, some deviations can clearly be noted in the the simulated XCH_4, caused by the relatively high initialization of background concentration fields. We discussed the diurnal variation of concentration components corresponding to different emission tracers for both CO_2 and CH_4. The biogenic component plays a pivotal and leading role in the variations of XCO_2. The impact from anthropogenic emission sources is somewhat weak compared to this, while for XCH_4, the enhancement over the background is dominated by human activities. There is little spatial difference in the biogenic contribution of CO_2 across all sites, while the anthropogenic contributions at the downwind sites are always higher than those at the upwind sites.

We then concentrated on using DCM for focusing our analysis on relevant CO_2 and CH_4 contributions from the urban area. DCM highlights that the enhancement of XCO_2 over background within the inner Berlin urban area is mostly caused by anthropogenic activities. In DCM, wind direction plays a vital role to define the upwind and downwind sites, which directly influence the calculation of differential column concentrations. In the CO_2 tracer analysis, it turns out that $\Delta\overline{\mathrm{XCO_2}}$, the difference with respect to a mean value instead of a specific upwind site, exhibits a more visible and clearer trend, which proves that the CO_2

enhancement over background is dominated by anthropogenic activities within the urban area. We conclude that DCM, when applied with care, helps to highlight the relevant emission sources. Similarly, for XCH_4, DCM eliminates the bias of the simulated values. Furthermore, when ΔXCH_4 values suffer from inconsistent wind directions, we consider $\Delta\overline{XCH_4}$ to be a useful quantity for analysis. The variations of $\Delta\overline{XCH_4}$ with time for simulations and measurements show encouraging agreement on 1st July, especially for Lichtenrade.

An analysis of XCO_2 in the Paris hot-spot region was carried out by Vogel et al. (2018). Some of their results can be compared to the conclusions we drew in this paper. In Vogel et al. (2018), the modelled XCO_2 was calculated based on the chemistry transport model CHIMERE (2 km) and flux framework CAMS (15 km), with hourly anthropogenic emissions from the IER and EDGAR emission inventories, and the natural fluxes prescribed by the S-TESSEL model (Sect.2 in Vogel et al. (2018)). When comparing results from our simulation, the diurnal variation in the XCO_2 enhancement over background (Sect.3.4 and Fig.4(a) of our paper) is comparable to the findings of Vogel et al. (2018). For the analysis on the comparison of ΔXCH_4 between simulations and measurements in Sect.4.1, we found that negative column concentration differences between down- and upwind sites appear for some periods, owing to the variation of wind directions that causes the conversion of up- and downwind sites, which was also mentioned for the ΔXCO_2 analysis in Vogel et al. (2018). Based on the CHIMERE-CAMS modelling framework, they showed that the strong decrease in XCO_2 during daytime can be linked to net ecosystem exchange, while a significant enhancement compared to the background is caused by XCO_2 from fossil fuel emissions, but this is often compensated by net ecosystem exchange. We utilized DCM to bring out the role of anthropogenic activities within urban areas (see the XCO_2 tracer analysis in Sect.4 of our paper).

We conclude that WRF-GHG is a suitable basis for precise GHG transport analysis in urban areas, especially when combined with DCM. DCM is not only useful for the direct evaluation of measurements, but also helps us to understand the results of tracer transport models, canceling out the bias caused, e.g., by initialization conditions, and highlighting regional emission sources.

In future work, we suggest running WRF-GHG for more urban areas, such that, e.g., different transport, topography and emission scenarios can be studied. The WRF-GHG mesoscale simulation framework may also be combined with microscale atmospheric transport models to simulate crucial details of emission sources and transport patterns precisely, with the aim of tracing urban GHG emissions. A further promising direction for future studies may be the application of DCM and model-based analysis to satellite measurements, to assess gradients across column concentrations with a dense spatial sampling.

Author contributions.

Xinxu Zhao performed the simulations, with the support and guidance of Julia Marshall, Christoph Gerbig and Jia Chen. Julia Marshall provided the CAMS fields for the initialization. Jia Chen supplied anthropogenic emission source and Christoph Gerbig offered the VPRM used for the simulations. Stephan Hachinger provided the guidance related to the running of the simulations in the Linux Cluster. Xinxu Zhao, Jia Chen and Stephan Hachinger designed the computational framework. Xinxu

Zhao and Jia Chen performed the analysis of the results. Xinxu Zhao wrote the manuscript with input from all authors. All authors provided critical feedback and helped shape the research, analysis and manuscript.

Data availability.

The simulation data that support the findings of this study are available on request from the corresponding author. The measurement data are available at doi:10.5194/amt-8-3059-2015 (Hase et al., 2015).

Competing interests.

The authors declare that they have no conflict of interest.

Acknowledgements. We thank Frank Hase for providing the measurement data for Berlin in 2014 and fruitful discussions. Jia Chen is partly supported by Technische Universität München – Institute for Advanced Study, funded by the German Excellence Initiative and the European Union Seventh Framework Programme under grant agreement no. 291763. The simulations presented in this work have been run on the Linux Cluster (CooLMUC-2) of the Leibniz Supercomputing Centre (LRZ, Garching).

Atmos. Chem. Phys. Discuss., https://doi.org/10.5194/acp-2018-1116
Manuscript under review for journal Atmos. Chem. Phys.
Discussion started: 16 January 2019

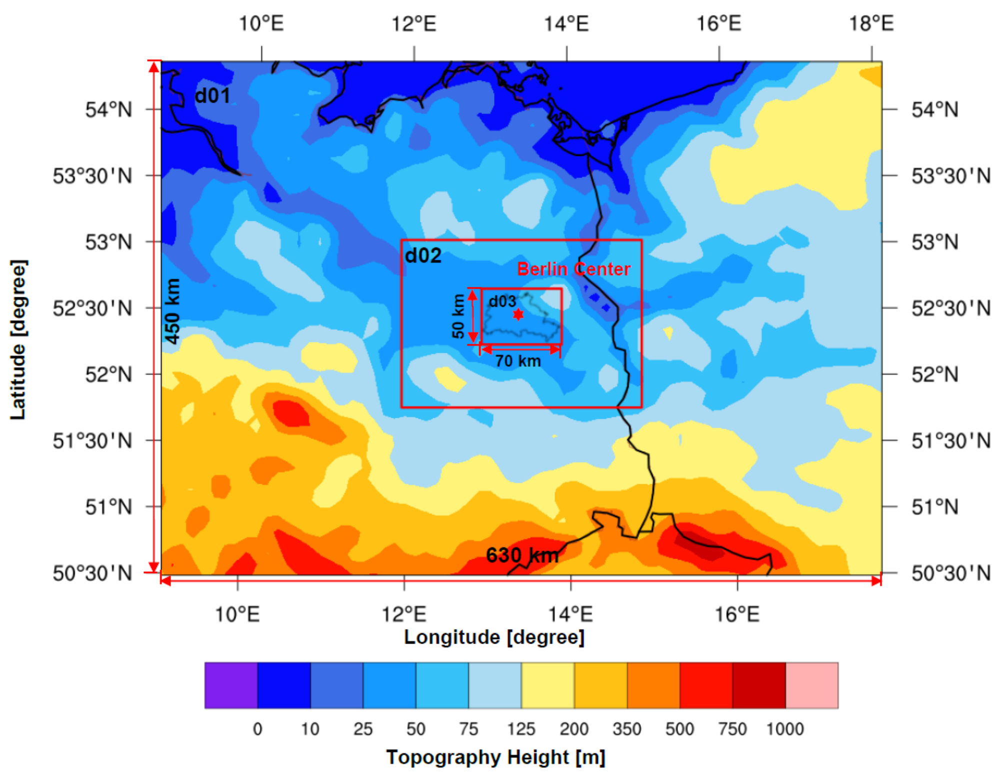

Figure 1. The topography map for the three domains in our study. The domain d03 is centered over Berlin, at 13.383°N, 52.517°E, marked with a red star. The boundary of Berlin from GADM (available at https://gadm.org/) is depicted in the innermost domain.

Atmos. Chem. Phys. Discuss., https://doi.org/10.5194/acp-2018-1116
Manuscript under review for journal Atmos. Chem. Phys.
Discussion started: 16 January 2019

Atmospheric Chemistry and Physics
Open Access
Discussions

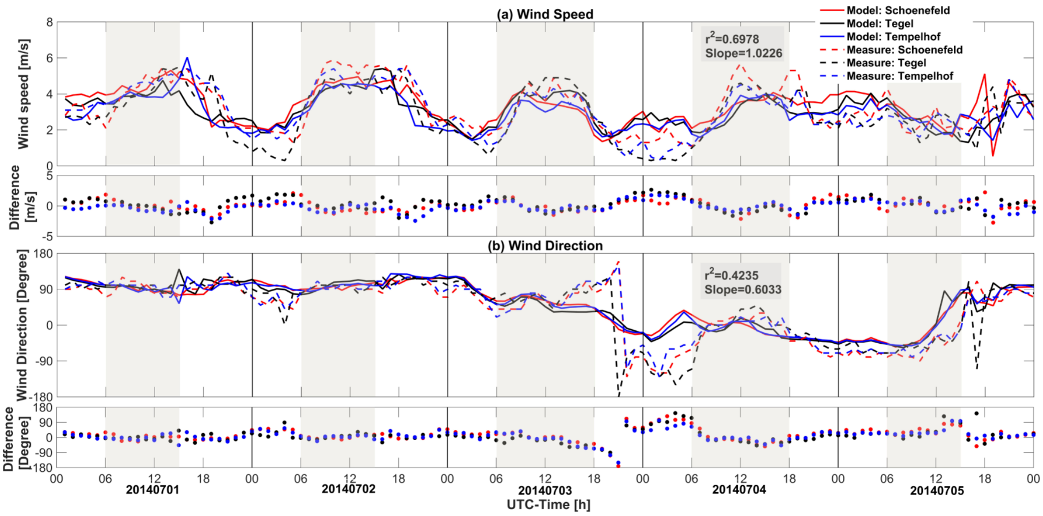

Figure 2. Variation and differences between simulated and measured wind fields for (a) wind speeds and (b) wind directions from 1st to 5th July 2014 at the three measurement sites, Schönefeld (red lines), Tegel (black) and Tempelhof (blue) in Berlin. The solid lines represent the simulated wind fields provided by WRF-GHG and the dashed lines depict the measured wind fields. The differences in (a)&(b) are simulations minus measurements. FTS measurement time periods on each date are marked by gray shaded areas.

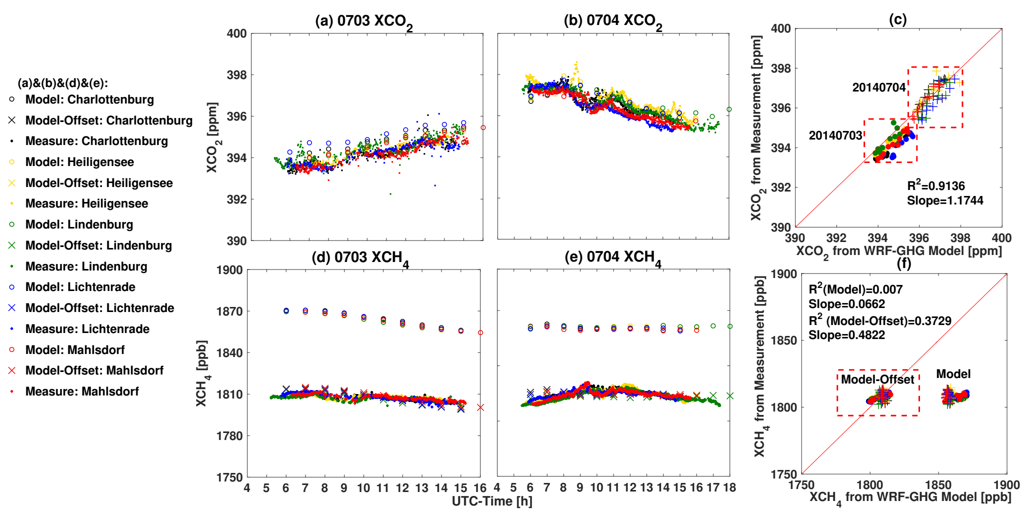

Figure 3. Variations and scatter plots of the measured and simulated XCO_2 and XCH_4 on 3rd and 4th July 2014, for five sampling sites in Berlin: Charlottenburg (black markers), Heiligensee (yellow), Lindenberg (green), Lichtenrade (blue) and Mahlsdorf (red). (a) XCO_2 on 3rd July; (b) XCO_2 on 4th July; (c) scatter plot for XCO_2; (d) XCH_4 on 3rd July; (e) XCH_4 on 4th July; (f) scatter plot for XCH_4. (a),(b),(d)&(e): The hollow circles stand for the simulated values provided by WRF-GHG and the solid circles represent the measured concentrations. The "x" markers in (d)&(e) represent the simulated XCH_4 after the subtraction of the daily offset. (c)&(f): The solid circles and the cross symbols represent the scatter plot points on 3rd and 4th July , respectively.

Atmos. Chem. Phys. Discuss., https://doi.org/10.5194/acp-2018-1116
Manuscript under review for journal Atmos. Chem. Phys.
Discussion started: 16 January 2019

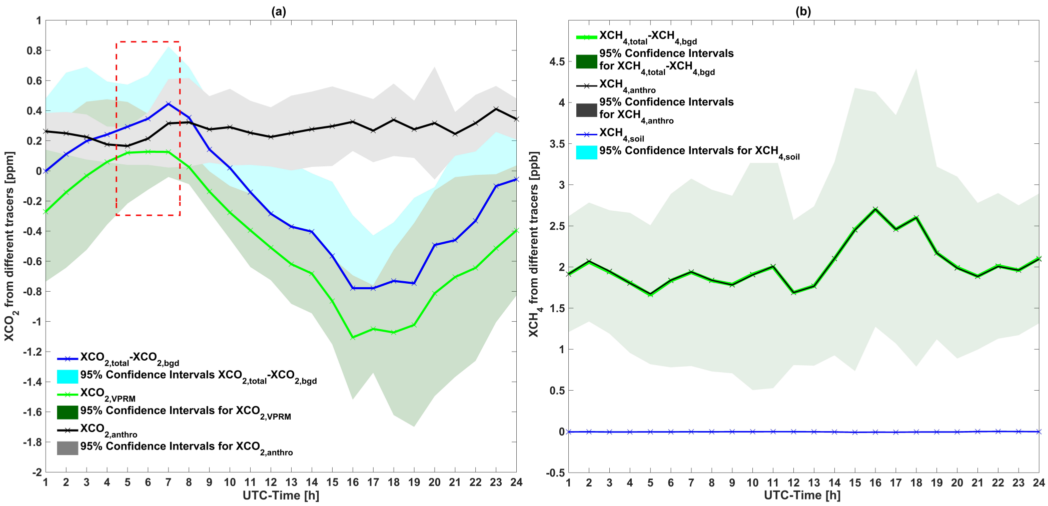

Figure 4. The diurnal variations of the simulated changes in concentrations caused by different emission tracers in Charlottenburg in Berlin from 2014, averaged over a period of nine days (from 2nd to 10th July 2014). The colored lines represent the concentration changes and the mean enhancement over background. (a): the mean hourly $XCO_{2,VPRM}$ (green line) and $XCO_{2,anthro}$ (black); (b): the mean hourly $XCH_{4,anthro}$ (black) and $XCH_{4,soil}$ (blue). The red box in (a) marks the morning peak of the XCO_2 enhancement over the background, as described in Sect.3.4.

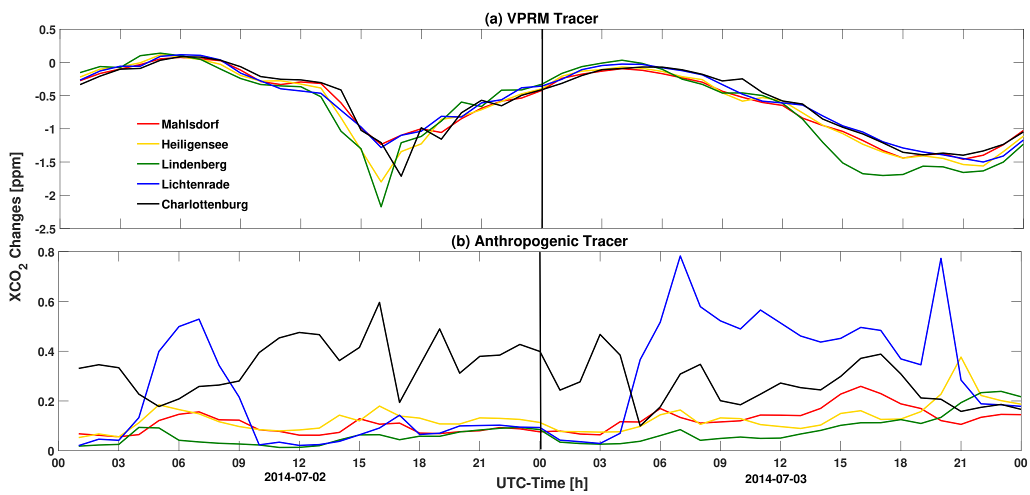

Figure 5. The diurnal variations of XCO_2 changes related to (a) VPRM and (b) anthropogenic tracers for five sampling sites on 2nd (left side) and 3rd (right) July 2014.

Atmos. Chem. Phys. Discuss., https://doi.org/10.5194/acp-2018-1116
Manuscript under review for journal Atmos. Chem. Phys.
Discussion started: 16 January 2019

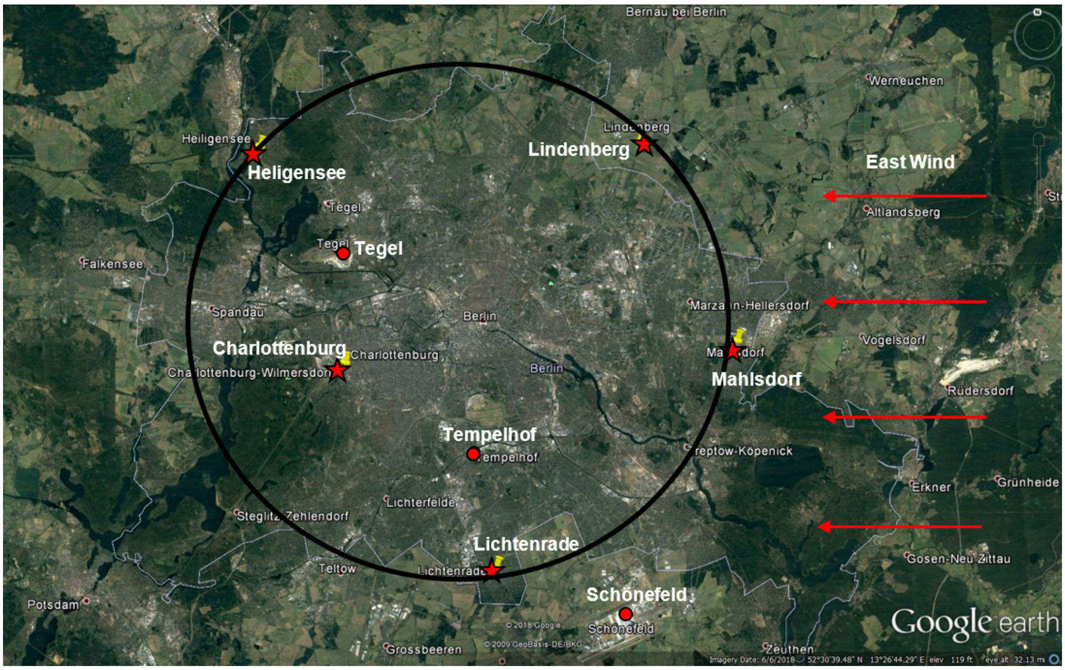

Figure 6. Detailed locations of the five sampling sites.The five red stars stand for the five sampling sites, four of which (Mahlsdorf, Heiligensee, Lindenberg and Lichtenrade) were roughly situated along a circle with a radius of 12 km around the center of Berlin, marked as the black circle. The innermost domain of our WRF-GHG model contains all five measurement sites. The three wind measurement sites are marked by red circles. Map provided by Google Earth.

Atmos. Chem. Phys. Discuss., https://doi.org/10.5194/acp-2018-1116
Manuscript under review for journal Atmos. Chem. Phys.
Discussion started: 16 January 2019

Atmospheric Chemistry and Physics
Discussions

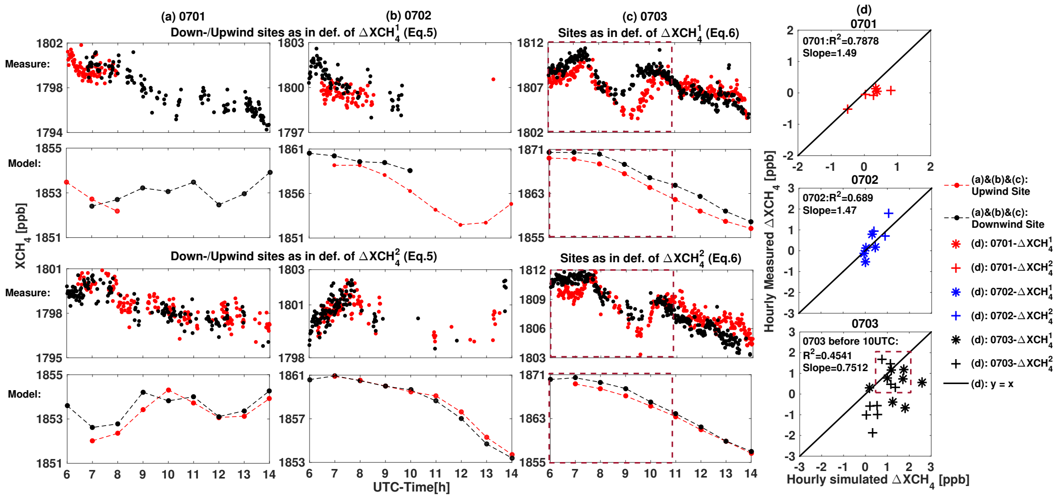

Figure 7. Downwind-minus-upwind differential evaluation of measured and simulated XCH_4 on 1st, 2nd and 3rd July 2014. (a),(b)&(c): XCH_4 at the downwind sites (black dots) and upwind sites (red dots); (d): scatter plot – simulated vs. measured hourly mean ΔXCH_4 for the three dates. In columns (a,b,c) we display the data for one date each; in the upper versus the lower two rows (for each date) we show the data with different choices for up-/downwind sites. These choices correspond to the definitions of ΔXCH_4^1 and ΔXCH_4^2 in the main text – Eq. 5 (1st & 2nd July) / Eq. 6 (3rd July). A red box in (c)&(d) marks values for the period before 10 UTC (cf. discussion in text).

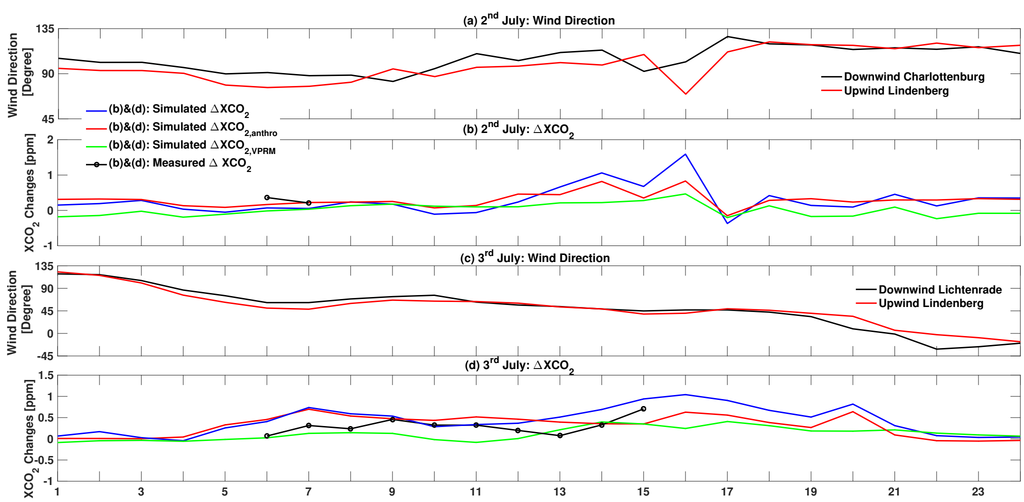

Figure 8. Wind directions and ΔXCO_2 on (a)&(b): 2nd and (c)&(d): 3rd July 2014. The ΔXCO_2 calculated using Eq.7 are depicted by blue lines in (b)&(d). The red and green lines in (b)&(d) show the variation of the differences between downwind and upwind sites in XCO_2 changes from anthropogenic and biogenic activities, respectively, while the black lines in (b)&(d) represent the variations of the measured ΔXCO_2 for these two days.

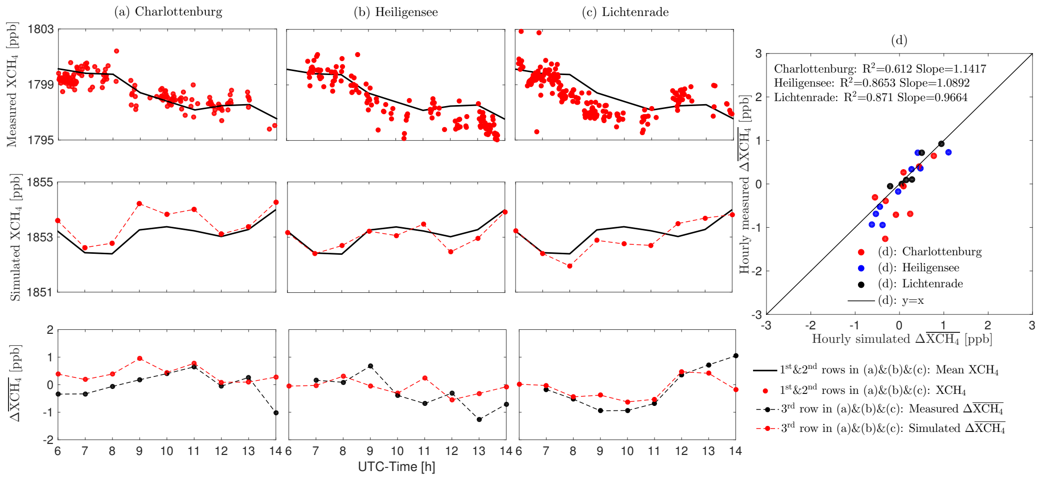

Figure 9. Site XCH_4 vs. site-mean XCH_4 data (1st row: measurements, 2nd row: simulations) for three sampling sites: Charlottenburg (column (a)), Heiligensee (b), and Lichtenrade (c). In the 3rd row, we compare the measured and simulated $\Delta\overline{XCH_4}$ values, i.e. the differential ("site minus site-mean") values (cf. Eq. 8, main text). Column (d) is a scatter plot of simulated vs. measured hourly mean $\Delta\overline{XCH_4}$ values.

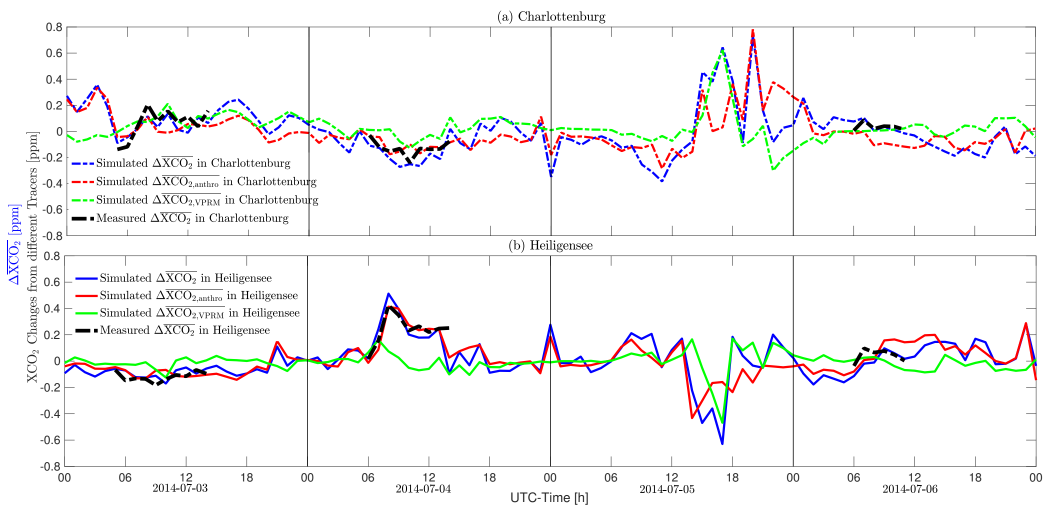

Figure 10. $\Delta\overline{XCO_2}$ (blue lines for simulations and black for measurements) for two specific sampling sites ((a) Charlottenburg, (b) Heiligensee), i.e. the difference between XCO_2 at the site and the mean XCO_2 of five sampling sites. We furthermore show the differences in the simulated XCO_2 changes from biogenic (green) and anthropogenic (red) activities on 3rd,4th,5th and 6th July 2014. No measured $\Delta\overline{XCO_2}$ is available on 5th July, due to the limited measurement data coverage.

Appendix A: WRF-GHG running process

A detailed description on how to run WRF-GHG is provided in Beck et al. (2011), and thus, only the initialization process for our study in particular is summarized here. One daily simulation with WRF-GHG is normally performed for a 30-hour time period including a 6-hour spin up for the meteorology from 18 UTC to 24 UTC of the previous day and a 24-hour simulation of the tracer transport on the actual simulation day (Beck et al., 2011).

As for the boundary conditions, a small constant offset needs to be added into the WRF boundary files for the biospheric CO_2 and the soil sink CH_4 tracers at the start of each run, because these tracers can result in a net sink. When the concentrations become negative, the advected tracer fields will "disappear", as the WRF code does not allow tracers with negative values. An offset applied in the initialization process helps to avoid this problem and later is subtracted in the post-processing. As for the initial conditions, the meteorological conditions are initialized with external data sources (GFS in our model) each day to update the WRF meteorological fields properly. The tracers for the total and background CO_2 and CH_4 flux fields are initialized only once, at the first day of the simulation period, using CAMS as an external data source. Furthermore, the lateral boundary conditions of the outer domain d01 is also initialized by the CAMS. Then, for the other days within the simulation period, these tracers for the total and background CO_2 and CH_4 fluxes are directly taken from the final WRF output at 24 UTC of the previous day to make the entire simulation continuous. The CO_2 tracer for VPRM and the CH_4 tracer for soil uptake are also initialized with a constant offset to avoid the appearance of negative values caused, e.g., by the vegetation respiration (Beck et al., 2011). In terms of the other flux tracers, the tracer variables are initialized each day, using external data sources to provide the updated emission data for each tracer.

Appendix B: Model systematic equation errors for Eq.1

In the passive tracer transport simulation, the total concentration of each GHG is represented as a separate tracer, giving redundant information (with respect to the sum of all tracers for each GHG), allowing for consistency checks. A variety of flux models and emission inventories implemented in the modules of WRF-GHG are used for the estimation of GHG fluxes. The flux values from external emission inventories are gridded and ingested into the model. In the transport process, the relationship among the changes in concentrations from different emission tracers, the total and background concentrations (Eq.1) should then be satisfied; ideally with $\Delta\mathrm{CO_2}$ and $\Delta\mathrm{CH_4}$ computational errors during the simulation process being zero. Nonzero values of $\Delta\mathrm{CO_2}$ and $\Delta\mathrm{CH_4}$ reflect the limited precision of the tracer transport calculation in WRF-GHG.

Figure.B1 thus shows the mean values (solid lines) and the 95 % confidence intervals of $\Delta\mathrm{CO_2}$ and $\Delta\mathrm{CH_4}$. As depicted in the figure, $\Delta\mathrm{CO_2}$ ranges from -0.005 ppm to 0.01 ppm while $\Delta\mathrm{CH_4}$ is in range of -0.01 ppb to 0.02 ppb. Divided by typical absolute values of the concentrations from different flux processes for XCO_2 (around 1 ppm) and XCH_4 (around 2-3 ppb) depicted in Fig.4, the relative computational error is found to be $\sim$1 % for both CO_2 and CH_4.

These tiny computational errors can be caused by the slight non-linearity of the advection scheme used in the WRF-GHG model, which makes the sum of the concentrations in CO_2 and CH_4 from all individual flux tracers not exactly equal to the concentration from the "sum tracer", representing the total sum of all fluxes related to different processes.

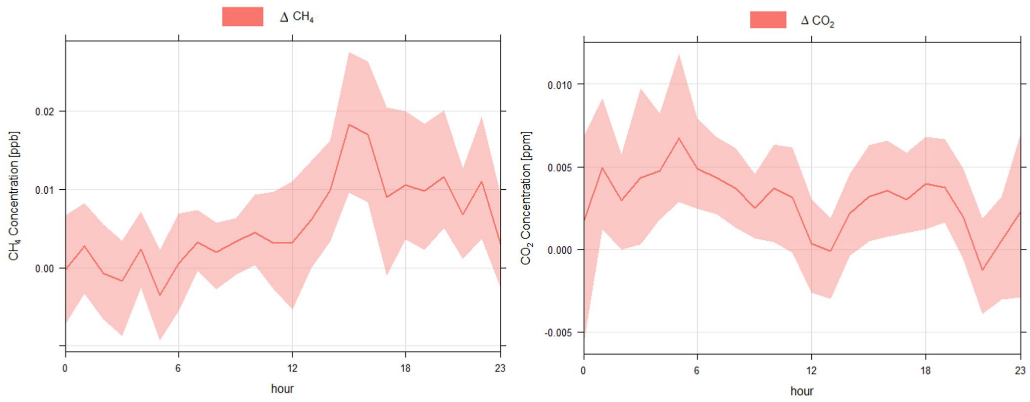

Figure B1. The mean values (solid lines) and the 95 % confidence intervals of the computational error ΔCO_2 (left) and ΔCH_4 (right). ΔCO_2 and ΔCH_4 are calculated using Eq.1.

Appendix C: The vertical distribution of CH_4 in CAMS

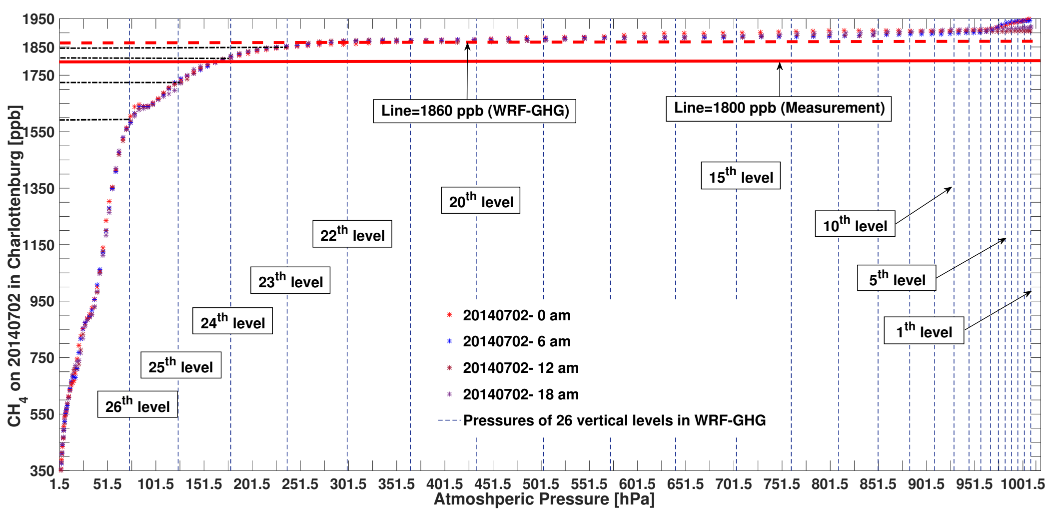

Figure C1. The vertical distribution of CH_4 on 2nd July in Charlottenburg. The asterisks represent the XCH_4 field from CAMS. The vertical dashed lines show the values of atmospheric pressure corresponding to the 26 vertical levels in our WRF-GHG. Y-axis levels of 1800 ppb and 1860 ppb, corresponding to the total column measurement and the modeled value, respectively, have been marked by red horizontal (solid / dashed) lines.

References

Agusti-Panareda, A., Diamantakis, M., Bayona, V., Klappenbach, F., and Butz, A.: Improving the inter-hemispheric gradient of total column atmospheric CO_2 and CH_4 in simulations with the ECMWF semi-Lagrangian atmospheric global model, Geoscientific Model Development, 10, 1–18, https://doi.org/10.5194/gmd-10-1-2017, 2017.

Ahmadov, R., Gerbig, C., Kretschmer, R., Koerner, S., Neininger, B., Dolman, A., and Sarrat, C.: Mesoscale covariance of transport and CO_2 fluxes: Evidence from observations and simulations using the WRF-VPRM coupled atmosphere-biosphere model, Journal of Geophysical Research: Atmospheres, 112, https://doi.org/10.1029/2007JD008552, 2007.

Ahmadov, R., Gerbig, C., Kretschmer, R., Körner, S., Rödenbeck, C., Bousquet, P., and Ramonet, M.: Comparing high resolution WRF-VPRM simulations and two global CO_2 transport models with coastal tower measurements of CO_2, Biogeosciences, 6, 807–817, https://doi.org/10.5194/bg-6-807-2009, 2009.

Andres, R. J., Boden, T. A., Bréon, F.-M., Ciais, P., Davis, S., Erickson, D., Gregg, J. S., Jacobson, A., Marland, G., Miller, J., et al.: A synthesis of carbon dioxide emissions from fossil-fuel combustion, Biogeosciences, 9, 1845–1871, https://doi.org/10.5194/bg-9-1845-2012, 2012.

Beck, V., Koch, T., Kretschmer, R., Marshall, J.and Ahmadov, R., Gerbig, C., Pillai, D., and Heimann, M.: The WRF Greenhouse Gas Model (WRF-GHG). Technical Report No. 25, Max Planck Institute for Biogeochemistry, Jena, Germany., 2011.

Bergamaschi, P., Corazza, M., Karstens, U., Athanassiadou, M., Thompson, R. L., Pison, I., Manning, A., Bousquet, P., Segers, A., Vermeulen, A., et al.: Top-down estimates of European CH_4 and N_2O emissions based on four different inverse models, Atmospheric Chemistry and Physics, 15, 715–736, https://doi.org/10.5194/acp-15-715-2015, 2015.

Caulton, D. R., Shepson, P. B., Santoro, R. L., Sparks, J. P., Howarth, R. W., Ingraffea, A. R., Cambaliza, M. O., Sweeney, C., Karion, A., Davis, K. J., et al.: Toward a better understanding and quantification of methane emissions from shale gas development, Proceedings of the National Academy of Sciences, p. 201316546, https://doi.org/10.1073/pnas.1316546111, 2014.

Chen, F., Kusaka, H., Bornstein, R., Ching, J., Grimmond, C., Grossman-Clarke, S., Loridan, T., Manning, K. W., Martilli, A., Miao, S., et al.: The integrated WRF/urban modelling system: development, evaluation, and applications to urban environmental problems, International Journal of Climatology, 31, 273–288, https://doi.org/10.1002/joc.2158, 2011.

Chen, J., Samra, J., Gottlieb, E., Budney, J., Wofsy, S. C., McKain, K., Hase, F., Gerbig, C., Chance, K., and McManus, J.: Novel instrumentation for column measurements and regional eulerian modeling for network design in Boston, in: AGU Fall Meeting Abstracts, 2013.

Chen, J., Viatte, C., Hedelius, J. K., Jones, T., Franklin, J. E., Parker, H., Gottlieb, E. W., Wennberg, P. O., Dubey, M. K., and Wofsy, S. C.: Differential column measurements using compact solar-tracking spectrometers, Atmospheric Chemistry and Physics, 16, 8479–8498, https://doi.org/10.5194/acp-16-8479-2016, 2016.

Chen, J., Dietrich, F., Franklin, J. E., Jones, T. S., André, B., Luther, A., Kleinschek, R., Hase, F., Wenig, M., Ye, S., Nouri, A., Frey, M., Knote, C., Alberti, C., and Wofsy, S.: Mesoscale column network for assessing GHG and NOx emissions in Munich, EGU General Assembly Conference Abstracts, Vol.20, EGU2018-10192-2, Vienna, Austria, 8–13 April 2018, https://meetingorganizer.copernicus.org/EGU2018/EGU2018-10192-2.pdf, 2018.

Cressot, C., Chevallier, F., Bousquet, P., Crevoisier, C., Dlugokencky, E., Fortems-Cheiney, A., Frankenberg, C., Parker, R., Pison, I., Scheepmaker, R., et al.: On the consistency between global and regional methane emissions inferred from SCIAMACHY, TANSO-FTS, IASI and surface measurements, Atmospheric Chemistry and Physics, 14, 577–592, https://doi.org/10.5194/acp-14-577-2014, 2014.

Deutscher, N. M., Notholt, J., Messerschmidt, J., Weinzierl, C., Warneke, T., Petri, C., Grupe, P., and Katrynski, K.: TCCON data from Bialystok (PL), Release GGG2014R1, TCCON data archive, hosted by CaltechDATA, https://doi.org/10.14291/tccon.ggg2014.bialystok01.R1/1183984, https://tccondata.org, 2014.

Fragkias, M., Lobo, J., Strumsky, D., and Seto, K. C.: Does size matter? Scaling of CO_2 emissions and US urban areas, PLoS One, 8, e64 727, https://doi.org/10.1371/journal.pone.0064727, 2013.

Franklin, J. E., Jones, T. S., Chen, J., Parker, H., Hedelius, J., Wennberg, P., Dubey, M. K., Cohen, Ron C., G. A., Sargent, M., Davis, K. J., Mielke, L., Fischer, M., and Wofsy, S.: A three-dimensional observation network for determining urban emissions of CO_2 and CH_4, 2017 North American Carbon Program, North Bethesda, MD, USA, https://www.nacarbon.org/meeting_2017/abs_and_discussions/mtg2017_ab_searchab_id161.html, 2017.

Fraunhofer-Gesellschaft: ISE: Map of Power Plants| Energy Chart, data source: European Energy Exchange (EEX), https://www.energy-charts.de/osm.htm, assessed August 14th, 2018, 2018.

Friedl, M. A., Sulla-Menashe, D., Tan, B., Schneider, A., Ramankutty, N., Sibley, A., and Huang, X.: MODIS collection 5 global land cover: Algorithm refinements and characterization of new datasets, 2001-2012, Collection 5.1 IGBP Land Cover, Boston University, Boston, MA, USA, 2010.

Gerbig, C., Körner, S., and Lin, J.: Vertical mixing in atmospheric tracer transport models: error characterization and propagation, Atmospheric Chemistry and Physics, 8, 591–602, https://doi.org/10.5194/acp-8-591-2008, 2008.

Hase, F., Frey, M., Blumenstock, T., Groß, J., Kiel, M., Kohlhepp, R., Mengistu Tsidu, G., Schäfer, K., Sha, M., and Orphal, J.: Application of portable FTIR spectrometers for detecting greenhouse gas emissions of the major city Berlin, Atmospheric Measurement Techniques, 8, 3059–3068, https://doi.org/10.5194/amt-8-3059-2015, 2015.

Hedelius, J. K., Viatte, C., Wunch, D., Roehl, C. M., Toon, G. C., Chen, J., Jones, T., Wofsy, S. C., Franklin, J. E., Parker, H., et al.: Assessment of errors and biases in retrievals of XCO_2, XCH_4, XCO, and XN_2O from a 0.5 cm–1 resolution solar-viewing spectrometer, Atmospheric Measurement Techniques, 9, 3527–3546, https://doi.org/10.5194/amt-9-3527-2016, 2016.

Holmes, C. D.: Methane Feedback on Atmospheric Chemistry: Methods, Models, and Mechanisms, Journal of Advances in Modeling Earth Systems, 10, 1087–1099, https://doi.org/10.1002/2017MS001196, 2018.

Hopkins, F. M., Ehleringer, J. R., Bush, S. E., Duren, R. M., Miller, C. E., Lai, C.-T., Hsu, Y.-K., Carranza, V., and Randerson, J. T.: Mitigation of methane emissions in cities: How new measurements and partnerships can contribute to emissions reduction strategies, Earth's Future, 4, 408–425, https://doi.org/10.1002/2016EF000381, 2016.

IEA: (International Energy Agency).: World Energy Outlook 2008, https://www.iea.org/media/weowebsite/2008-1994/WEO2008.pdf, 2008.

IEA: International Energy Agency :Cities, Towns & Renewable Energy, Tech. rep., http://www.iea.org/publications/freepublications/publication/cities2009.pdf, 2009.

IPCC: (International Panel on Climate Change).: IPCC fifth assessment report: Climate change 2014 Synthesis Report. Summary for Policymakers, http://www.ipcc.ch/pdf/assessment-report/ar5/syr/AR5_SYR_FINAL_SPM.pdf, 2014.

Janssens-Maenhout, G., Crippa, M., Guizzardi, D., Dentener, F., Muntean, M., Pouliot, G., Keating, T., Zhang, Q., Kurokawa, J., Wankmüller, R., et al.: HTAP_v2: a mosaic of regional and global emission gridmaps for 2008 and 2010 to study hemispheric transport of air pollution., Atmospheric Chemistry and Physics, 15, 11 411–11 432, https://doi.org/10.5194/acp-15-11411-2015, 2015.

Kennedy, C., Steinberger, J., Gasson, B., Hansen, Y., Hillman, T., Havranek, M., Pataki, D., Phdungsilp, A., Ramaswami, A., and Mendez, G. V.: Greenhouse gas emissions from global cities, 43, 7297–7302, https://doi.org/10.1021/es900213p, 2009.

Kindler, A., Klimeczek, H.-J., and Franck, U.: Socio-spatial distribution of airborne outdoor exposures–An indicator for environmental quality, quality of life, and environmental justice: The case study of Berlin, in: Urban Transformations, pp. 257–279, Springer, https://doi.org/10.1007/978-3-319-59324-1_14, 2018.

Kivi, R. and Heikkinen, P.: Fourier transform spectrometer measurements of column CO_2 at Sodankylä, Finland, Geoscientific Instrumentation, Methods and Data Systems, 5, 271–279, https://doi.org/10.5194/gi-5-271-2016, 2016.

Kretschmer, R., Gerbig, C., Karstens, U., and Koch, F.-T.: Error characterization of CO_2 vertical mixing in the atmospheric transport model WRF-VPRM, Atmospheric Chemistry and Physics, 12, 2441–2458, https://doi.org/10.5194/acp-12-2441-2012, 2012.

Mahadevan, P., Wofsy, S. C., Matross, D. M., Xiao, X., Dunn, A. L., Lin, J. C., Gerbig, C., Munger, J. W., Chow, V. Y., and Gottlieb, E. W.: A satellite-based biosphere parameterization for net ecosystem CO_2 exchange: Vegetation Photosynthesis and Respiration Model (VPRM), Global Biogeochemical Cycles, 22, https://doi.org/10.1029/2006GB002735, 2008.

Marcotullio, P. J., Sarzynski, A., Albrecht, J., Schulz, N., and Garcia, J.: The geography of global urban greenhouse gas emissions: An exploratory analysis, Climatic Change, 121, 621–634, https://doi.org/10.1007/s10584-013-0977-z, 2013.

McKain, K., Wofsy, S. C., Nehrkorn, T., Eluszkiewicz, J., Ehleringer, J. R., and Stephens, B. B.: Assessment of ground-based atmospheric observations for verification of greenhouse gas emissions from an urban region, Proceedings of the National Academy of Sciences, 109, 8423–8428, https://doi.org/10.1073/pnas.1116645109, 2012.

Montzka, S. A., Dlugokencky, E. J., and Butler, J. H.: Non-CO_2 greenhouse gases and climate change, Nature, 476, 43–50, https://doi.org/10.1038/nature10322, 2011.

Muntean, M., Janssens-Maenhout, G., Song, S., Selin, N. E., Olivier, J. G., Guizzardi, D., Maas, R., and Dentener, F.: Trend analysis from 1970 to 2008 and model evaluation of EDGAR.V4 global gridded anthropogenic mercury emissions, Science of the Total Environment, 494, 337–350, https://doi.org/10.1016/j.scitotenv.2014.06.014, 2014.

Newman, S.and Xu, X., Gurney, K. R., Hsu, Y. K., Li, K. F., Jiang, X., Keeling, R., Feng, S., O'Keefe, D., Patarasuk, R., Wong, K. W., Rao, P., Fischer, M. L., and Yung, Y. L.: Toward consistency between trends in bottom-up CO_2 emissions and top-down atmospheric measurements in the Los Angeles megacity, Atmospheric Chemistry and Physics, 16, 3843–3863, https://doi.org/10.5194/acp-16-3843-2016, 2016.

Notholt, J., Petri, C., Warneke, T., Deutscher, N. M., Buschmann, M., Weinzierl, C., Macatangay, R., and Grupe, P.: TCCON data from Bremen (DE), Release GGG2014R0, TCCON data archive, hosted by CaltechDATA, https://doi.org/10.14291/tccon.ggg2014.bremen01.R0/1149275, https://tccondata.org, 2014.

Ohyama, H., Morino, I., Nagahama, T., Machida, T., Suto, H., Oguma, H., Sawa, Y., Matsueda, H., Sugimoto, N., Nakane, H., and Nakagawa, K.: Column-averaged volume mixing ratio of CO_2 measured with ground-based Fourier transform spectrometer at Tsukuba, Journal of Geophysical Research: Atmospheres, 114, https://doi.org/10.1029/2008JD011465, 2009.

Olsen, S. C. and Randerson, J. T.: Differences between surface and column atmospheric CO_2 and implications for carbon cycle research, Journal of Geophysical Research: Atmospheres, 109, https://doi.org/10.1029/2003JD003968, 2004.

Ostler, A., Sussmann, R., Patra, P. K., Houweling, S., De Bruine, M., Stiller, G. P., Haenel, F., Plieninger, J., Bousquet, P. J., Yin, Y., Saunois, M., Walker, K. A., Deutscher, N. M., Griffith, D. W. T., Blumenstock, T., Hase, F., Warneke, T., Wang, Z., Kivi, R., and Robinson, J.: Evaluation of column-averaged methane in models and TCCON with a focus on the stratosphere, Atmospheric Measurement Techniques, 9, 4843–4859, https://doi.org/10.5194/amt-9-4843-2016, 2016.

Parshall, L., Gurney, K., Hammer, S. A., Mendoza, D., Zhou, Y., and Geethakumar, S.: Modeling energy consumption and CO_2 emissions at the urban scale: Methodological challenges and insights from the United States, Energy Policy, 38, 4765–4782, https://doi.org/10.1016/j.enpol.2009.07.006, 2010.

Pillai, D., Gerbig, C., Ahmadov, R., Rödenbeck, C., Kretschmer, R., Koch, T., Thompson, R., Neininger, B., and Lavrié, J.: High-resolution simulations of atmospheric CO_2 over complex terrain–representing the Ochsenkopf mountain tall tower, Atmospheric Chemistry and Physics, 11, 7445–7464, https://doi.org/10.5194/acp-11-7445-2011, 2011.

Pillai, D., Gerbig, C., Kretschmer, R., Beck, V., Karstens, U., Neininger, B., and Heimann, M.: Comparing lagrangian and eulerian models for CO_2 transport - a step towards Bayesian inverse modeling using WRF/STILT-VPRM, Atmospheric Chemistry and Physics, 12, 8979–8991, https://doi.org/10.5194/acp-12-8979-2012, 2012.

Pillai, D., Buchwitz, M., Gerbig, C., Koch, T., Reuter, M., Bovensmann, H., Marshall, J., and Burrows, J. P.: Tracking city CO_2 emissions from space using a high-resolution inverse modeling approach: a case study for Berlin, Germany, Atmospheric Chemistry and Physics, 16, 9591–9610, https://doi.org/10.5194/acp-16-9591-2016, 2016.

Reusswig, F.and Hirschl, B. and Lass, W.: Climate-Neutrality Berlin 2050: Results of a Feasibility Study, Tech. rep., Senate Department for Urban Development and the Environment, https://www.berlin.de/senuvk/klimaschutz/studie_klimaneutrales_berlin/download/Machbarkeitsstudie_Berlin2050_EN.pdf, 2014.

Saikawa, E., Kim, H., Zhong, M., Avramov, A., Zhao, Y., Janssens-Maenhout, G., Jurokawa, J., Klimont, Z., Wagner, F., Naik, V., et al.: Comparison of emissions inventories of anthropogenic air pollutants and greenhouse gases in China, Atmospheric Chemistry and Physics, 17, 6393–6421, https://doi.org/10.5194/acp-17-6393-2017, 2017.

SenStadtH: Berlin Environmental Atlas: 06.01 Actual Use of Built-up Areas/ 06.02 Inventory of Green and Open Spaces/ 06.01.1 Actual Use / 06.02.1 Actual Use and Vegetation Cover (Edition 2016), http://www.stadtentwicklung.berlin.de/umwelt/umweltatlas/e_text/eke601.pdf, 2016.

Skamarock, William C.and Klemp, J. B., Dudhia, J., Gill, D. O., Barker, D. M., Duda, M. G., Huang, X.-Y., Wang, W., and Powers, J. G.: Description of the Advanced Research WRF Version 3, Tech. rep., National Center for Atmospheric Research, https://pdfs.semanticscholar.org/ace5/4d4d1d6c9914997ad8f4e410044fdeb95b9d.pdf, 2008.

Skamarock, W. C., Klemp, J. B., Dudhia, J., Gill, D. O., Barker, D. M., Wang, W., and Powers, J. G.: A description of the advanced research WRF Version 2, Tech. rep., National Center For Atmospheric Research Boulder Co Mesoscale and Microscale Meteorology Div, 2005.

Toja-Silva, F., Chen, J., Hachinger, S., and Hase, F.: CFD simulation of CO_2 dispersion from urban thermal power plant: Analysis of turbulent Schmidt number and comparison with Gaussian plume model and measurements, Journal of Wind Engineering and Industrial Aerodynamics, 169, 177–193, https://doi.org/10.1016/j.jweia.2017.07.015, 2017.

UNDESA: (United Nations Department of Economic and Social Affairs).: World Urbanization Prospects: The 2014 Revision, https://esa.un.org/unpd/wup/Publications/, 2014.

UNDESA: (United Nations Department of Economic and Social Affairs).: World Urbanization Prospects: The 2018 Revision, https://esa.un.org/unpd/wup/Publications/, 2018.

Viatte, C., Lauvaux, T., Hedelius, J. K., Parker, H., Chen, J., Jones, T., Franklin, J. E., Deng, A. J., Gaudet, B., Verhulst, K., Duren, R., Wunch, D., Roehl, C., Dubey, M., Wofsy, S., and Wennberg, P.: Methane emissions from dairies in the Los Angeles Basin, Atmospheric Chemistry and Physics, 17, 7509–7528, https://doi.org/10.5194/acp-17-7509-2017, 2017.

Vogel, F. R., Frey, M., Staufer, J., Hase, F., G., B., Xueref-Remy, I., Chevallier, F., Ciais, P., Sha, M. K., Chelin, P., Jeseck, P., Janssen, C., Te, Y.-V., Groß, J., Blumenstock, T., Tu, Q., and Orphal, J.: XCO_2 in an emission hot-spot region: the COCCON Paris campaign 2015, Atmos. Chem. Phys. Discuss., in review, https://doi.org/10.5194/acp-2018-595, 2018.

Wang, H., Fu, L., Lin, X., Zhou, Y., and Chen, J.: A bottom-up methodology to estimate vehicle emissions for the Beijing urban area, Science of the total environment, 407, 1947–1953, 2009.

Wu, L., Broquet, G., Ciais, P., Bellassen, V., Vogel, F., Chevallier, F., Xueref-Remy, I., and Wang, Y.: What would dense atmospheric observation networks bring to the quantification of city CO_2 emissions?, Atmospheric Chemistry and Physics, 16, 7743–7771, https://doi.org/10.5194/acp-16-7743-2016, 2016.

Wunch, D., Toon, G. C., Blavier, J.-F. L., Washenfelder, R. A., Notholt, J., Connor, B. J., Griffith, D. W., Sherlock, V., and Wennberg, P. O.: The total carbon column observing network, Philosophical Transactions of the Royal Society of London A: Mathematical, Physical and Engineering Sciences, 369, 2087–2112, https://doi.org/10.1098/rsta.2010.0240, 2011.